Effect of Radar Incident Angle on Full-Wave Inversion for the Retrieval of Medium Surface Permittivity for Drone-Borne Applications

Kaijun Wu and Sébastien Lambot, *Member, IEEE*

***Abstract*— Drone-borne ground-penetrating radar (GPR) has proven to be efficient and promising for high-resolution topsoil moisture mapping at the field scale. However, in practice, the radar incident angle may change as a function of the terrain slope and unstable flying conditions. In this respect, we analyzed the effect of radar incident angle on full-wave inversion for soil permittivity characterization. Specifically, using the frequency-domain radar equation, antenna characteristic functions with different incident angles were determined for a horn antenna as an example. Then, numerical analyses and field measurements were performed to quantify the errors on the retrieved permittivity resulting from incident angle drifts. In agreement with the radar equation concept, we observed that the angle- and frequency-dependent global transmission functions of the antenna correspond well to its radiation pattern. Numerical and field results show that errors in the permittivity estimation can be very significant as a function of the antenna radiation pattern and the incident angle. Nevertheless, if the incident angle is known and the characteristic antenna functions are determined as a function of the incident angle, full-wave modeling and inversion remain accurate, provided that the signal-to-noise ratio remains sufficient.**

***Index Terms*— Dielectric permittivity, drone, full-wave inversion, ground-penetrating radar (GPR), incident angle, radiation pattern.**

I. Introduction

With drone technology developments, a growing number of new possibilities are now available for various scientific research and applications. Lightweight ground-penetrating radar (GPR) systems are also considered promising to be used on drones for different purposes. Drone-borne and airborne GPRs have been successfully used for surface and subsurface imaging, for target detection with different geometric shapes and properties, and for digital soil mapping. However, the radar incident angle is always an important factor to be considered in applications of combining drone and GPR. Catapano *et al.* [1] considered the incident and refraction angles in the scattering phenomenon modeling for buried object imaging using helicopter-borne GPR. Chandra and Tanzi [2] proposed employing slantwise incidence for a specific surface medium, with an assumption of the drone-borne GPR radiating at Brewster incidence, to transmit the incident power preferentially and maximally. For a GPR system made of a receiver mounted on a drone with its transmitter placed on a vehicle looking forward, the incident angle makes the image distort [3]. Similarly, the incident and refraction angles are considered for elevation correction in detecting low reflective targets using drone-GPR [4]. The backscattering coefficient of the synthetic aperture radar (SAR) is affected by the incident angle, so two incident angles were applied to incorporate the roughness effects on soil moisture mapping [5], [6].

The antenna radiation pattern and the incident angle play, indeed, an important role in radar applications. In telecommunications, the antenna radiation pattern affects the received signal strength and delay spreads in wireless communication systems [7], [8]. The receiving antenna radiation pattern has an impact on the coverage in the single-frequency network, e.g., directive antennas decrease the self-interference [9]. In airborne SAR imaging, extended pulses of sidelobes lead to distortions [10], while some radiation pattern width or beamwidth is needed in circular aperture synthesis for object image reconstruction [11] and the Doppler noncontact vibration-detection radar system [12]. Incident angles bring errors in hyperspectral LiDAR laser scanning due to variations of specular reflection and laser footprint [13]. For on-ground GPR, Reppert *et al.* [14] used Brewster angles to determine the velocity below the deepest detectable reflector. Similar to the amplitude variation with angle (AVA) method in seismic exploration [15], the critical angle is important to be considered for the velocity analysis, the wide-angle common midpoint (CMP) surveys, AVA, and the refraction method [16]–[18]. In addition, the radiation patterns might have negative effects on GPR data imaging. Better imaging for the amplitude and phase of reflection can be achieved when antenna radiation patterns are taken into account [19], [20].

In off-ground GPR applications, especially for the system with only one antenna acting as transmitter and receiver, the radiation pattern mainly determines spatial resolution, as greater directivity is better for receiving stronger reflection and discriminating closely spaced targets. Ludeno *et al.* [21]

Manuscript received October 20, 2021; revised January 24, 2022; accepted March 2, 2022. Date of publication March 8, 2022; date of current version April 12, 2022. This work was supported in part by the Politique Scientifique Fédérale (BELSPO, Belgium) in the frame of the Research Programme for Earth Observation STEREO III, RAPAS Project under Contract SR/00/238 and in part by the Fonds de la Recherche Scientifique (FNRS, Belgium). *(Corresponding author: Kaijun Wu.)*

The authors are with the Earth and Life Institute, Université Catholique de Louvain, 1348 Leuven-la-Neuve, Belgium (e-mail: kaijun.wu@student.uclouvain.be).

Digital Object Identifier 10.1109/TGRS.2022.3157370

used antennas with relatively wide radiation patterns for microwave tomography radar imaging. Gennarelli *et al.* [22] used a log-periodic antenna whose gain is 7 dB of a beamwidth 68° for wide-area geophysical surveys. Transmitting and receiving antennas with wide and relatively homogeneous radiation patterns were used in order to have a negligible effect on data accuracy [23].

Recently, we developed a new frequency-domain drone-borne GPR consisting of a homemade transverse electromagnetic (TEM) horn antenna for soil moisture measurement [24]. For data processing, the radar equation introduced by Lambot *et al.* [25], [26] was used to model the radar signal, including antenna effects, and then perform signal inversion to retrieve the medium properties. This radar equation is commonly used under the condition where the antenna aperture is parallel with the medium surface. Yet, for drone applications, the incident angle inherently changes as a function of the soil topography and flying conditions. As the radiation pattern of antennas is not homogeneous, this is expected to result in inversion errors if it is not accounted for in the radar model. The drone-GPR application is not widespread yet, especially for topsoil electromagnetic properties measurement (the relative dielectric permittivity and electrical conductivity). The incident angle may not be an issue for other air-launched GPR applications (e.g., hyperbola recognition and radar imaging), but it may significantly affect the full-wave inversion for medium surface characterization by influencing the amplitude of the surface reflection.

In this article, we analyze how the incident angle affects full-wave inversion for retrieving medium permittivity from the surface reflection. First, following the radar equation, the frequency-dependent global reflection and transmission coefficients of a double-ridged horn antenna were determined for a range of different incident angles [25], [26]. The global transmission functions were then compared to the radiation patterns of the antenna, as determined by the manufacturer. Then, these functions were used to simulate radar data for varying incident angles and medium permittivity. These data were subsequently inverted assuming normal incidence, thereby permitting quantifying inversion errors when the incident angle is not normal and not accounted for in the forward model. Finally, tests were performed in real field conditions, including inversion accounting for the incident angle to avoid estimation errors. Although the presented analyses focus on one antenna as an example, they remain valid for any type of antenna given the physics behind the radar equation and the full-wave model. Just the quantitative results would be different depending on the particular radiation pattern of the antenna.

II. Methodology

A. Radar Equation

A radar antenna matches the characteristic impedance of the feed line with the intrinsic impedance of the medium, so there are variations of impedance between the radar reference plane, where the field is measured, and the antenna aperture or effective phase center, e.g., 50 Ω of the feed line to 120π Ω of the free space for air-launched GPR. This variation can be linear, exponential, or follow more complex functions, including discontinuities and so on [27], [28]. The received radar signal contains all the effects resulting from these antenna impedance variations, which are unwanted and, especially, should be accounted for in inversion methods for medium characterization. The closed-form frequency-domain radar equation accounts for these effects and, in far-field conditions, is expressed in the frequency domain as [25], [26]

$$S_{11}(\omega,\Theta) = R_i(\omega) + \frac{T_s(\omega,\Theta)G_{xx}(\omega)T_i(\omega,\Theta)}{1 - G_{xx}(\omega)R_s(\omega,\Theta)}. \tag{1}$$

In this equation, ω is the angular frequency, we introduce in this article Θ as the incident angle (as shown in Fig. 1), and $\Theta = [\theta_{\mathrm{H}}, \theta_{\mathrm{E}}]$, denoting the incident angles in H- and E-planes, respectively. S_{11} is measured directly by the vector network analyzer (VNA). G_{xx} is the Green's function defined as the x component of the backscattered electric field for a unit, x-directed electric source for wave propagation in 3-D planar layered media. R_i, R_s, T_s, and T_i are the antenna characteristic functions. R_i is the global reflection coefficient of the antenna for fields incident from the radar reference plane onto the source point or the return loss. $R_i = S_{11}$ in free space conditions for which $G_{xx} = 0$. Hence, S_{11} depends on the incident angle as it depends on the antenna transfer functions, which depends themselves on the incident angle. R_i does not depend on the incidence angle, and in this article, we also consider G_{xx} to be independent on the incident angle assuming an x-directed point source. R_s is the global reflection coefficient of the antenna for fields incident from the antenna phase center (backscattered field) onto the radar reference plane. T_s is the global transmission coefficient for fields incident from the field points onto the radar reference plane, while T_i is the global transmission coefficient for fields incident from the radar reference plane onto the field points. T_s and T_i are mathematically correlated with each other, so we can only estimate T_sT_i, and we define accordingly $T(\omega,\Theta) = T_s(\omega,\Theta)T_i(\omega,\Theta)$ as the antenna transmitting–receiving response function. It is well-known that the antenna radiation pattern is a representation of the distribution of the power radiated from or received to the antenna as a function of direction angles [27]. Similarly, $T(\omega,\Theta)$ can be seen as the radiation pattern of the antenna expressed in terms of the global transmission coefficient in the radar equation.

B. Full-Wave Inversion

The inverse problem is defined using the least-squares formulation. Inversion is conducted in the time domain, and the objective function is expressed as

$$\phi(\mathbf{b}) = \left(\mathbf{g}_{xx}^*(t) - \mathbf{g}_{xx}(\mathbf{b},t)\right)^{\mathsf{T}}\left(\mathbf{g}_{xx}^*(t) - \mathbf{g}_{xx}(\mathbf{b},t)\right) \tag{2}$$

where $\mathbf{g}_{xx}^*(t)$ and $\mathbf{g}_{xx}(\mathbf{b},t)$ are, respectively, the measured (or simulated) and modeled Green's function vectors and obtained by inverse Fourier transform of $G_{xx}(\omega)$, so t denotes the time. Performing inversion in the time domain allows focusing on a

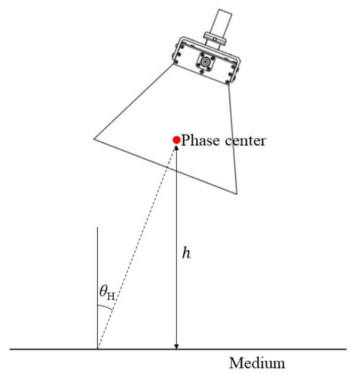

(a)

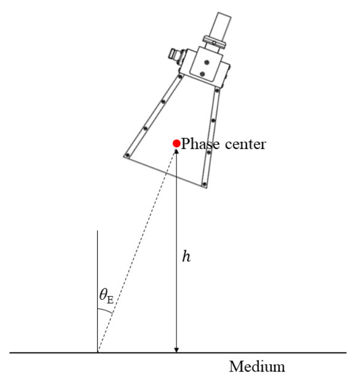

(b)

Fig. 1. Model configurations in (a) H-plane and (b) E-plane. h is the distance between the phase center and the medium. θ_{H} and θ_{E} denote the incident angles in the H- and E-planes, respectively. (Antenna drawing is from Schwarzbeck Mess-Elektronik, Germany. http://www.schwarzbeck.com/en/antennas/broadband-horn-antennas/double-ridged-horn-antenna.html.)

time window, e.g., corresponding to the surface reflection only. **b** is the parameter vector $[h_m,\ \varepsilon_{r,m}]$, where h_m is the distance between the antenna phase center and the soil surface, and $\varepsilon_{r,m}$ is the medium relative permittivity, namely, the surface dielectric permittivity in this case. The electrical conductivity σ can be neglected in the frequency range that we operate if we focus on the surface reflection only [29]. Specifically, the apparent electrical conductivity of the soil can be neglected only if it is <100 mS/m depending on the frequency range. Also in the environment, it may not be satisfied in wet soils or soils with high clay content unless the frequency is high enough. A lookup table (LUT) is used for robust and fast inversion. Indeed, as there are two unknowns only, the objective function can be calculated in the full parameter space, and finding the minimum becomes, therefore, straightforward. In this study, $\mathbf{h}_m = [0.7\ 1.3]$ m with intervals of 0.005 m and $\varepsilon_{r,m} = [2\ 25]$ with intervals of 0.5 for both numerical and field experiments, resulting in 5687 parameter pairs for which the objective function is calculated.

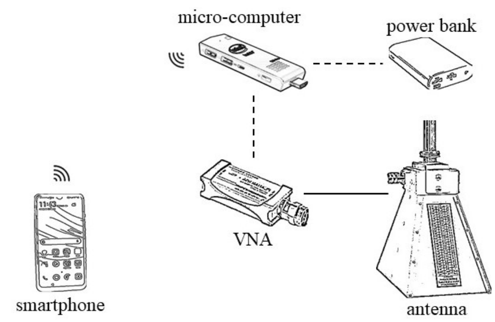

Fig. 2. Radar system diagram using the BBHA 9120-A horn antenna (Schwarzbeck Mess-Elektronik, Germany). The solid line denotes the direct connection between the connectors of the antenna and the VNA, and the dashed lines denote devices connection to the compute stick via USB.

III. Radar System

In the whole study, we use the BBHA 9120-A horn antenna (Schwarzbeck Mess-Elektronik, Germany) as an example. It is a linear polarized double-ridged horn antenna with a nominal frequency range from 0.8 to 5.2 GHz. The phase center was defined at 0.0714 m from the antenna aperture [30]. One antenna is used as the transmitter and the receiver at the same time.

The whole radar system is shown in Fig. 2. It consists of a lightweight VNA (Planar R54, Copper Mountain Technologies, Indianapolis, USA), an Intel compute stick, a power bank, and a smartphone as we used for drone-borne GPR [24]. Specifically, the USB-powered R54 VNA works as the radar system unit, setting up a stepped-frequency continuous-wave (SFCW) radar. It enables direct connection to the device under test (DUT), namely, the transmitting and receiving radar antennas in this case. The Intel compute stick operates in the Windows 10 system, providing a platform for controlling the radar unit. This computer is powered by a micro-USB connector fed with 5 V, i.e., a smartphone-type power bank. An application corresponding to the VNA is installed in the microcomputer, so the VNA is remotely controlled by means of user programs written with component object model (COM) technology. A smartphone is used separately by users to control the radar measurements. Python and Javascript programs were developed to remotely control the microcomputer. These programs are remotely triggered by the smartphone, and the smartphone is connected to the Intel compute stick through a hotspot launched by the smartphone itself. An HTTP server is set up using Node.js on the computer to provide the user interface.

IV. Antenna Calibration and Radiation Pattern

Antenna calibration is to calculate the antenna characteristic functions using the far-field frequency-domain radar equation as (1) [25]. It was conducted over a large copper sheet (3 m × 3 m) so that, in our frequency range, it can be assumed as an infinite plane in the electromagnetic (EM) model (Green's function). The measurement configurations are shown in Fig. 1. Measurements were carried out in the frequency range of 0.8–5.2 GHz with a step of 10 MHz. Nine angles were considered for both H- and E-planes, respectively ($\theta_{\mathrm{H/E}} = [0° \ 5° \ 10° \ 15° \ 20° \ 25° \ 30° \ 35° \ 40°]$). Please note that we use $\theta_{\mathrm{H/E}}$ instead of Θ here to clarify that we conducted the analyses separately in the H- and E-planes. For each angles, seven measurements with different distance h from the copper sheet were conducted in order to calculate the antenna characteristic functions [25], [31], and $h = [0.30 \ 0.31 \ 0.33 \ 0.36 \ 0.40 \ 0.45 \ 0.51]$ m. For both H- and E-planes, we collected 126 measurements ($S_{11}(\omega, \Theta)$ in (1)) in total (9 angles × 2 planes × 7 distances). $G_{xx}(\omega)$ was calculated through the frequency-domain Green's function using the known distance and the electromagnetic properties of the copper sheet assumed as a perfect electrical conductor. The antenna characteristic functions R_s, T, and T_s were obtained by solving a system of equations as (1).

To compare the antenna transmitting–receiving response function T and radiation pattern, we plot T in polar coordinates and formulate it in decibel (dB) as

$$T_{\mathrm{dB}}(\omega, \theta_{\mathrm{H/E}}) = 20\log_{10}\left(\frac{|T(\omega, \theta_{\mathrm{H/E}})|}{\max(|T(\omega, \theta_{\mathrm{H/E}}))|}\right) \quad (3)$$

in which $\max(|T(\omega, \theta_{\mathrm{H/E}}))|)$ is the maximum amplitude of $T(\omega, \theta_{\mathrm{H/E}})$ from the total nine angles, i.e., when $\theta_{\mathrm{H/E}} = 0°$ for this antenna. The antenna radiation pattern as determined by the manufacturer was generated from the original file of Schwarzbeck (http://schwarzbeck.de/Datenblatt/ri9120a.pdf). We used an online application WebPlotDigitizer 4.4 (https://apps.automeris.io/wpd/) to get the corresponding point values from the radiation pattern figures.

Fig. 3 shows the antenna characteristic functions in magnitude and phase when incident angles take place in the H-plane. The results are similar in the E-plane, so we do not present the transfer function in the E-plane here. As expected, the return loss R_i does not change with the incident angle. The feedback loss function R_s changes in an irregular way when the angle increases. This relatively complex behavior may be because the multiple reflectors constituted by the different parts of the antenna become progressively more complex and asymmetrical with the increasing angle.

The transmitting–receiving function T is of interest and importance in this study since it represents the strength of EM wave radiation with respect to angles, so it is equivalent to the antenna radiation pattern by definition. The antenna transmitting–receiving transfer functions and radiation pattern comparisons are shown in Fig. 4. We observe in Fig. 3(e) and (f) that the transmitting–receiving function T decreases with the increase in incident angle, and its phase also changes, especially at high frequencies. This corresponds, indeed, to the radiation pattern of the antenna (as presented in Fig. 4). For the directional antenna, it radiates or receives larger power in a specific direction, i.e., 0° direction in this case. In general, the transfer function T_{dB} agrees very well with the manufacturer radiation patterns. The observed differences can be attributed to the different measurement conditions in which these patterns were determined and to the fact that a different antenna EM model is used (including R_s in our case, as a more complete EM model).

V. Numerical Analyses

We conducted numerical analyses to investigate the incident angle effects on soil properties characterization using off-ground GPR and full-wave inversion, specifically for soil surface permittivity estimation. In the simulation model, we define the distance between the soil surface and the antenna aperture h as 1 m, and the medium relative permittivity ε_r is arbitrarily defined as 13, representing an average value for soils. The soil conductivity σ is defined as 0 mS/m since it does not affect the surface reflection in that frequency range assuming conductivity values of natural soils [29].

Fig. 5 sketches the generation of the simulated radar signals (Processing I) and the filtering of the antenna effects (Processing II). The simulated signals $S_{11,j}$ ($j = 1, 2, \ldots, 9$ refers to $\theta_{\mathrm{H/E}}) = [0° \ 5° \ 10° \ 15° \ 20° \ 25° \ 30° \ 35° \ 40°]$ as calibrated in the last section) were generated from synthetic Green's functions $G_{xx,s}(\omega)$ using (1) and angle-dependent antenna transfer functions (ATF_j). In practice, it is always assumed that the antenna aperture is parallel with the medium surface during measurement, so the antenna transfer functions of, i.e., ATF_1 ($R_i(\omega)$, $T_1(\omega)$ and $R_{s,1}(\omega)$), were used to filter $S_{11,j}$. Hereby, $G_{xx,j}$ is obtained as

$$G_{xx,j}(\omega) = \frac{S_{11,j}(\omega) - R_i(\omega)}{T_1(\omega) + S_{11,j}(\omega)R_{s,1}(\omega) - R_i(\omega)R_{s,1}(\omega)}. \quad (4)$$

Following our model assumptions in (1) with respect to Θ, in theory, G_{xx} should not depend on the incident angle, but, in this case, as the wrong model is used, i.e., ATF_1, G_{xx} becomes angle-dependent. We present an example of $G_{xx,j}$ in the frequency and time domains in Fig. 6. From the frequency domain Fig. 6(a), it is observed that the amplitude becomes extremely large at high frequencies when the incident angle increases to 5°–25°. When the incident angle is larger than 25°, the amplitude gets smaller. From the frequency domain Fig. 6(b), we observe that, when the incident angle increases, the wave peak amplitude of reflection decreases, and it becomes too weak to be recognized when the incident angle is larger than 25°. In addition, there are more variations when the incident angle is within 5°–25°, corresponding to the large amplitude at high frequencies observed in the frequency domain. This may be attributed to the rapidly varying field propagation paths within the antenna as a function of the angle when there are some small incident angles. Nevertheless, when the incident angle becomes too large, the transmitted and received waves become weak, which can be seen from the transmitting–receiving function presented in Fig. 3(e) and (f) or from the radiation patterns in Fig. 4.

The inversion results using different frequency ranges are presented in Fig. 7, including the full range 0.8–5.2 GHz and different subranges with a bandwidth of 0.6 GHz. As expected, errors in the estimation of the relative permittivity are inevitable when the incident angle in both the H- and E-planes is not accounted for in the inversion EM model, and the larger is the incident angle, the larger is the error produced. In addition, when the incident angle is not equal to 0°, the error increases with higher frequencies being used in the inversion. The inversion results of the relative permittivity ε_r using the full range 0.8–5.2 GHz are not satisfying

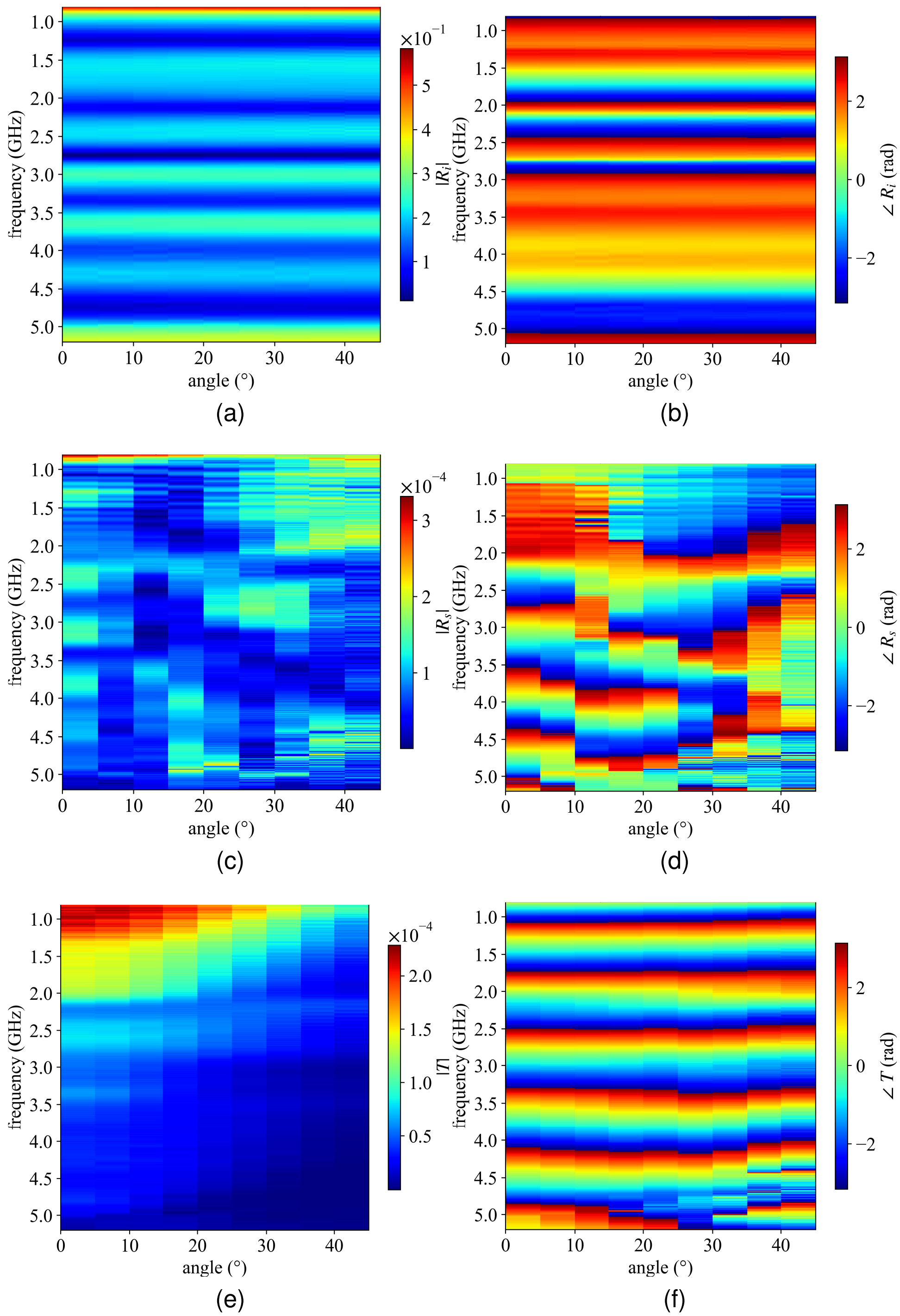

Fig. 3. Amplitude (a), (c), and (e), and phase (b), (d), and (f) of the antenna characteristic functions R_i (a) and (b), R_s (c) and (d), and T (e) and (f) as a function of the incident angle in the H-plane.

especially for the E-plane angles, as it drops rapidly even when the incident angle is only 5°. The increasing error in the estimation of permittivity with the increase in either the incident angle or the frequency ranges can be explained by the shape of the frequency-dependent radiation pattern and the antenna transmitting–receiving transfer function. Following the frequency-dependent antenna radiation pattern, the transmitted or received field decreases with the increase in incident angle, and it decreases more rapidly at higher frequencies (see Fig. 4). The amplitude of Green's function is sensitive to the operating frequency. Normally, at those frequencies, ε_r determines the amplitude of reflection, and the amplitude is directly affected by the angle-dependent antenna radiation pattern, which results in the wrong estimation of ε_r. Besides, the distance h was better retrieved than ε_r. This is to be attributed to the relatively small effect of the incidence angle on the two-way wave propagation time between the antenna and the medium. Yet, for a large angle, the error becomes significant due to the different geometry of the propagation model.

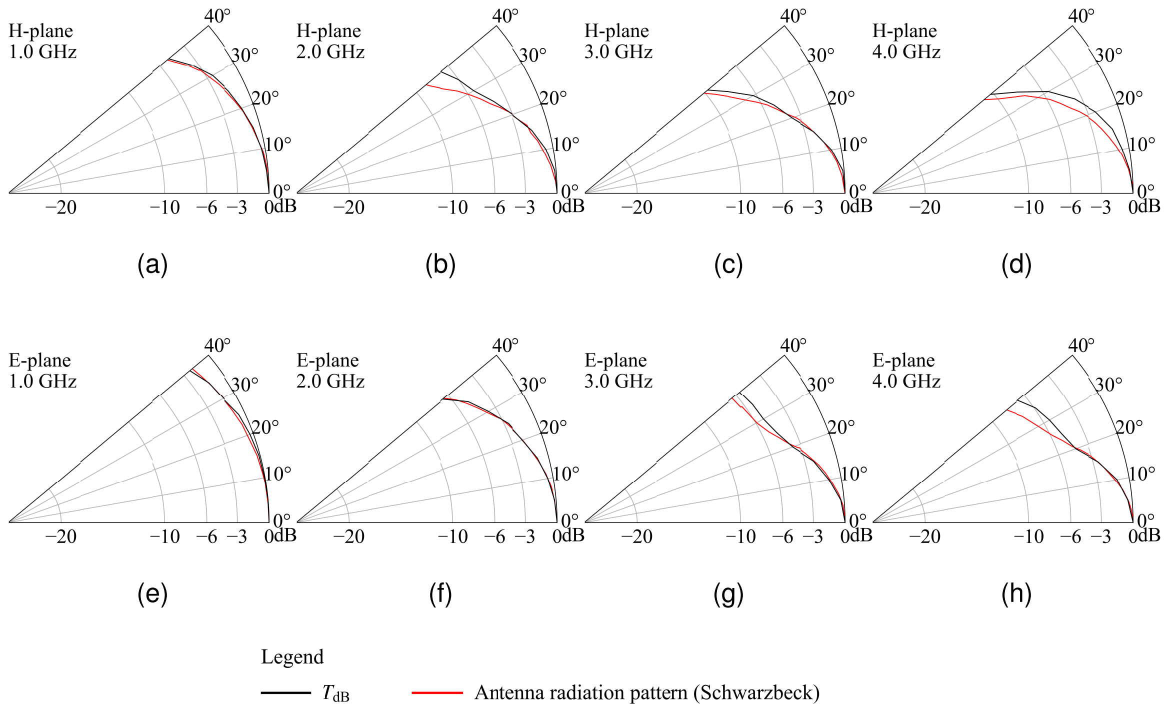

Fig. 4. Antenna transmitting–receiving transfer functions T_{dB} in amplitude and corresponding radiation patterns in the H- (a)–(d) and E-planes (e)–(h). BBHA 9120-A horn antenna (Schwarzbeck, Mess-Elektronik, Germany).

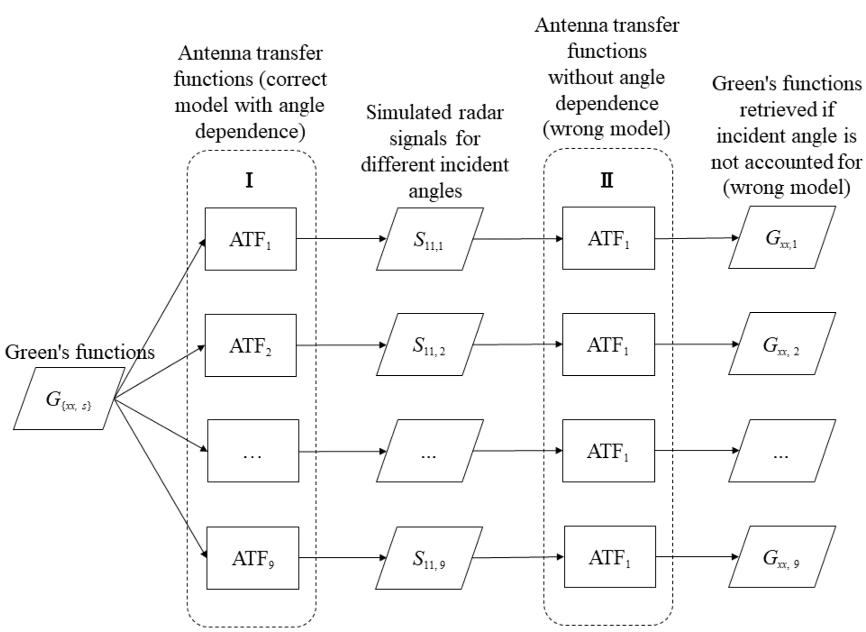

Fig. 5. Simulation signals' generation and antenna effects removal flowchart. $G_{xx,s}(\omega)$ is the synthetic Green's function in the frequency domain, corresponding to $G_{xx}(\omega)$ in (1). ATF_j represents the antenna transfer functions [including R_i, $T_j(\omega)$, and $R_{s,j}(\omega)$], where subscript $j = 1, 2, \ldots, 9$ refers to different transfer functions for different angles $\theta = 0°, 5°, \ldots, 40°$ in the H- and E-planes, respectively. Likewise, $S_{11,j}(\omega)$ and $G_{xx,j}(\omega)$ denote different simulated signals and filtered data for different angles. Processing I is the generation of simulation signals, and processing II is to filter out antenna effects using the wrong model (i.e., without angle dependence).

Therefore, in off-ground GPR measurement and inversion, it is necessary to keep as much as possible the antenna aperture parallel with the medium surface if angle dependence is not accounted for. It is worth noting that an antenna with a more homogeneous radiation pattern (less directive, such as a dipole) would lead to smaller errors.

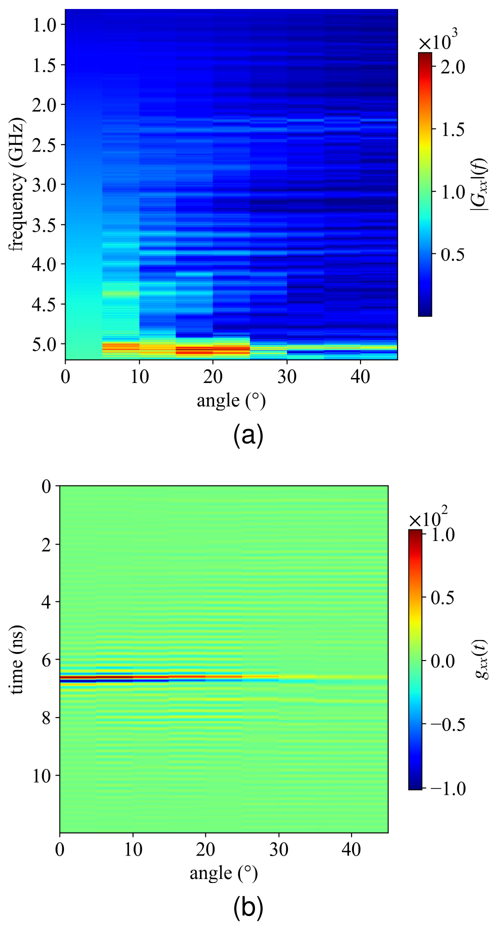

Fig. 6. Green's functions in (a) frequency domain and (b) time domain processed using ATF_1 in the H-plane ($G_{xx,j}$ in Fig. 5). In this example, the simulation parameters are $h = 1$ m and $\varepsilon_r = 13$.

VI. Field Experiments

Field measurements were performed over the soil with a short lawn in a flat garden (loamy soil). We did measurements over the same point. In both the H- and E-planes, we performed nine measurements with the angle varying from 0° to 40° with a step of 5°. The operating frequency range was 0.8–1.4 GHz with a step of 10 MHz. We choose this frequency range following the discussions in numerical experiments and importantly to avoid roughness and vegetation effects following Rayleigh's criterion [31]. For comparison, we conducted parameter inversion under two conditions, without and with the incident angle taken into account. For the former, the antenna effects were filtered using antenna transfer functions of 0°, i.e., ATF_1 (also see the Processing II in Fig. 5). For the latter, the antenna transfer functions in each angle ATF_j calibrated in Section IV were used to remove antenna effects from the signal measured with the corresponding angle so that the incident angle was considered in the data processing. Inversion model settings are the same as in numerical experiments.

The field experimental results are shown in Fig. 8. When ignoring the incident angle, in both the H- and E-planes, inversion provided the same ε_r value as 13 when the radar incident angle is 0°. Then, the error increases with the incident angle increasing. In the E-plane, the relative permittivity error for $\theta = 10°$ is still acceptable (depending on the application) with an absolute error of only 1.5 (absolute error $= |\varepsilon_r^* - \varepsilon_r|$, where ε_r^* is the estimated soil relative permittivity, and ε_r is the value obtained for normal incidence, considered as true), and in the H-plane, the absolute error reaches 3 for the same angle. Generally, results in the E-plane are better than in the H-plane for each angle. When the incident angle is taken into account (see the E- and H-plane$_\theta$ in Fig. 8), the results can be accurate within 0 to 25° with a maximum error of 2. However, the estimated ε_r is too large (e.g., $\theta \geq 30°$) even if the incident angle is considered.

For the results in E- and H-planes, such as the numerical experiments, it is explained by the antenna radiation pattern, that is: 1) the gain of antenna decreases with the increase in the incident angle and 2) within this frequency range, the gain decreases more rapidly in the E-plane than in the H-plane (e.g., see 1.0-GHz antenna radiation patterns in Fig. 4). For the results of E- and H-plane$_\theta$ curves in Fig. 8, when the incident angles were accounted for, the high estimated ε_r at large angles comes from the high amplitude in the calibrated Green's function at larger angles. From (4), since the return loss R_i does not depend on the incident angle and magnitude of R_s is around 10^{-4}, the decreasing of S_{11} leads to high amplitude of $G_{xx,\theta}$. When the incident angle increases, more and more EM waves are emitted toward the air instead of the medium surface, making S_{11} become closer to R_i ($S_{11} = R_i$ in free space conditions). Fig. 9 shows the amplitude of $S_{11} - R_i$ when S_{11} is measured in different incident angle conditions. We observe that the amplitude starts to drop at 25°, and it drops sharply when the incident angle is 40°. However, when an incident angle of 25° is considered, the estimation of ε_r is satisfying. In addition, it is also to be attributed to the antenna frequency response functions, mainly to the drop of the transmitting–receiving function T within the frequency range 0.8–2 GHz when the incident angle $\theta \geq 30°$ [see Fig. 3(c)] and partly to the feedback loss function R_s being high at large incident angles [see Fig. 3(e)]. These effects result in a too low signal-to-noise ratio (SNR). The high-amplitude noise contributes to the extra amplitude to the reflection, and then, ε_r is overestimated. The frequency-domain Green's functions for three angles in the H-plane are presented as examples (see Fig. 10), where each incident angle is taken into account. When the incident angle is too large (e.g., 40°), we observe that Green's function in the frequency domain contains higher local clutter.

In conclusion, the angle-dependent antenna radiation pattern significantly affects full-wave inversion for soil surface properties characterization resulting from transmitting and receiving less power for increasing angles. Besides, when the incident angle is taken into account, the medium permittivity can be retrieved through inverse modeling. What is more, there is also a limitation that the incident angle should not be too large to keep enough SNR. This limitation can be different depending on the antenna itself, the aperture, size, variation of impedance, and so on. The radar equation is theoretically valid for any incident angle. Yet, less satisfactory results may be obtained when the SNR becomes low for incident angles for which radiation toward the reflecting medium is low.

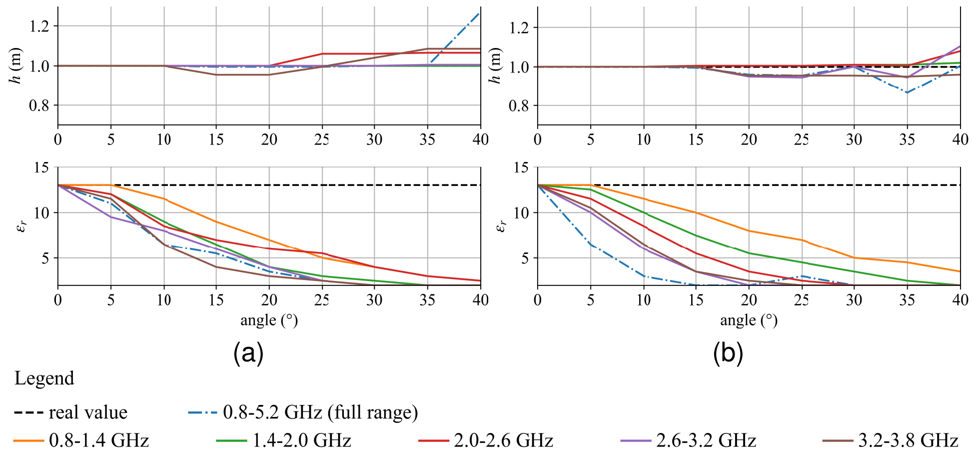

Fig. 7. Inversion results for the numerical experiments using different frequency ranges in (a) H-plane and (b) E-plane. In the simulation model, the distance between the antenna aperture and medium surface h is set as 1 m, and the medium relative permittivity ε_r is defined as 13. The legend denotes the frequency range used for inversion.

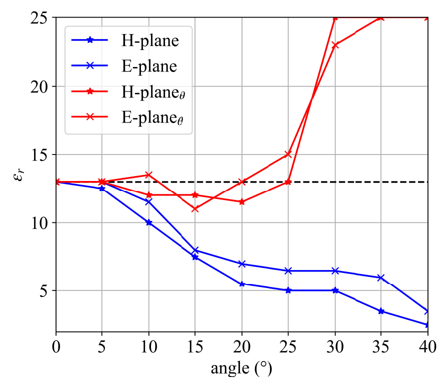

Fig. 8. Inverted relative permittivity as a function of the incident angle in both H- and E-planes for the field experiment. E- and H-planes denote the antenna effects removal without considering the incident angle in both planes. E- and H-plane$_\theta$ denote that the antenna effects are removed with the incident angle being taken into account.

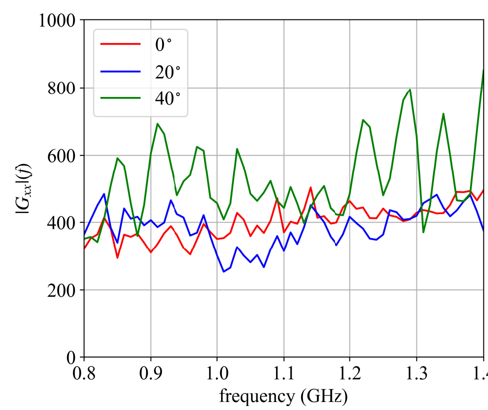

Fig. 10. Filtered Green's function in the frequency domain for the field data with the incident angle under consideration (the H-plane). The Green's functions of three angles (0°, 20°, and 40°) are presented for comparison.

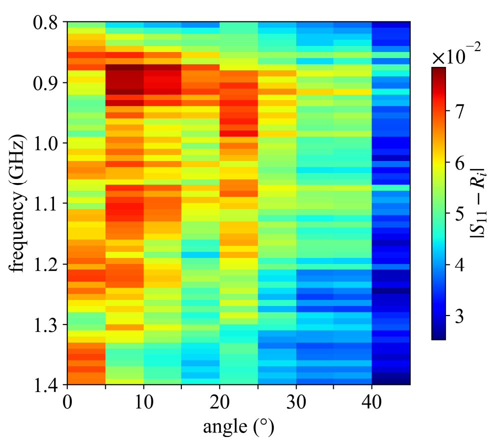

Fig. 9. Amplitude of measured $S_{11} - R_i$ for different incident angles in the H-plane as a function of frequency.

VII. Conclusion

In this article, we analyze the effect of the incident angle on full-wave inversion, and we include the incident angle in the frequency-domain radar equation [25], [26]. We show the comparison between the antenna radiation patterns and the antenna transmitting–receiving response functions for the first time. A relatively directive horn antenna is used as an example. Specifically, we compare antenna characteristic functions for different incident angles ranging from 0° to 40° with a step of 5°, and the frequency ranges from 0.8 to 5.2 GHz with a step of 10 MHz. The return loss response remains the same for each angle, while the feedback loss function and the transmitting–receiving function change with the incident angle. The most significant change is found in the transmitting–receiving transfer function. It decreases with the increase in incident angle, agreeing well with the antenna radiation pattern.

The numerical experiments show that the incident angle significantly affects the soil property characterization using the off-ground GPR and full-wave inversion method. To simulate the radar signal for each angle, we calculated Green's function and reformulated it using different antenna characteristic functions for each angle. In data processing, the antenna transfer functions of 0° are used to filter antenna effects out in order to neglect the incident angle. We compare the inversion results processed with different frequency ranges as well.

The estimations of the medium relative permittivity ε_r and the distance between antenna aperture and the medium surface h are not accurate when the incident angle is large. The estimation of h is better than that of ε_r. It becomes incorrect when the amplitude of reflection is too weak with respect to the SNR. Besides, for each angle, the higher operating frequency range leads to a larger estimation error. It is concluded that the antenna radiation pattern directly affects the amplitude of wave peak at specific directions and decreases more rapidly at higher frequencies for this antenna.

Finally, we measured the same soil in real field conditions with the incident angles ranging from 0° to 40° with a step of 5°. The measured data were processed using transfer functions of 0° and corresponding angles of 0°–40°. The results further show that the estimated soil permittivity decreases with the increase in the incident angle due to the transmitting–receiving transfer function decreasing, while small angles are accepted, e.g., 5° angle produces small absolute errors of 0.5 in the H-plane, and 10° produces only 1.5 in the E-plane for the relative permittivity. However, even if the incident angle is taken into account, errors cannot be neglected when the incident angle is too large.

This study extends the far-field frequency-domain antenna model introduced by Lambot *et al.* [25] for different incident angles. It also provides instructive information for future studies in the application of drone-borne GPR and full-wave inversion for soil surface properties characterization. It is necessary to either account for the incident angle or to use a less directional antenna, e.g., the half-wave dipole. It is worth noting that, with the model being fully physically based, the results of these analyses are valid for any type of antenna. Just the quantitative results will be different as a function of particular antenna radiation patterns.

References

[1] I. Catapano, L. Crocco, Y. Krellmann, G. Triltzsch, and F. Soldovieri, "A tomographic approach for helicopter-borne ground penetrating radar imaging," *IEEE Geosci. Remote Sens. Lett.*, vol. 9, no. 3, pp. 378–382, May 2012.

[2] M. Chandra and T. J. Tanzi, "Drone-borne GPR design: Propagation issues," *Comp. Rendus Phys.*, vol. 19, nos. 1–2, pp. 72–84, Jan. 2018.

[3] M. Garcia-Fernandez, A. Morgenthaler, Y. Alvarez-Lopez, F. Las Heras, and C. Rappaport, "Bistatic landmine and IED detection combining vehicle and drone mounted GPR sensors," *Remote Sens.*, vol. 11, no. 19, p. 2299, Oct. 2019.

[4] V. Kafedziski, S. Pecov, and D. Tanevski, "Integration of elevation correction with surface reflected wave removal for detection of low reflective targets in UAV mounted GPR systems," in *Proc. 14th Int. Conf. Adv. Technol., Syst. Services Telecommun. (TELSIKS)*, Oct. 2019, pp. 261–264.

[5] H. S. Srivastava, P. Patel, M. L. Manchanda, and S. Adiga, "Use of multiincidence angle RADARSAT-1 SAR data to incorporate the effect of surface roughness in soil moisture estimation," *IEEE Trans. Geosci. Remote Sens.*, vol. 41, no. 7, pp. 1638–1640, Jul. 2003.

[6] N. Baghdadi *et al.*, "Operational performance of current synthetic aperture radar sensors in mapping soil surface characteristics in agricultural environments: Application to hydrological and erosion modelling," *Hydrol. Processes*, vol. 22, no. 1, pp. 9–20, Jan. 2008.

[7] E. Coca and V. Popa, "Antenna radiation pattern influence on the localization accuracy in wireless sensor networks," *Adv. Electr. Comput. Eng.*, vol. 13, no. 2, pp. 43–46, 2013.

[8] A. K. M. Baki and S. Sharmin, "Effect of radiation patterns on WLAN delay spreads for 60 GHz living room environments," in *Proc. IEEE Int. Conf. Telecommun. Photon. (ICTP)*, Dec. 2017, pp. 67–71.

[9] P. J. Orbea, J. M. Matias, M. Hernandez, Y. Valdes, and S. Landeros, "Effect of receiving antennas radiation pattern on an SFN network coverage," in *Proc. IEEE Symp. Comput. Commun. (ISCC)*, Jun. 2019, pp. 1–7.

[10] G. Sharma and A. B. Raj, "Effects of antenna radiation pattern on airborne SAR imaging with sufficient cyclic prefix-OFDM," in *Proc. IEEE 4th Conf. Inf. Commun. Technol. (CICT)*, Dec. 2020, pp. 1–6.

[11] V. P. Yushchenko and S. A. Litvinenko, "Effect of the radiation pattern on the quality of object image reconstruction in circular aperture synthesis," *Optoelectron., Instrum. Data Process.*, vol. 52, no. 4, pp. 328–333, Jul. 2016.

[12] C.-M. Nieh, T.-Y. Huang, and J. Lin, "Antenna radiation pattern effects on a short-range vibration-detection radar system," in *Proc. Int. Symp. Antennas Propag. Conf.*, Dec. 2014, pp. 135–136.

[13] W. Tian *et al.*, "Analysis and radiometric calibration for backscatter intensity of hyperspectral LiDAR caused by incident angle effect," *Sensors*, vol. 21, no. 9, p. 2960, Apr. 2021.

[14] P. M. Reppert, F. D. Morgan, and M. N. Toksöz, "Dielectric constant determination using ground-penetrating radar reflection coefficients," *J. Appl. Geophys.*, vol. 43, nos. 2–4, pp. 189–197, Mar. 2000.

[15] A. D. Booth, E. Emir, and A. Diez, "Approximations to seismic AVA responses: Validity and potential in glaciological applications," *Geophysics*, vol. 81, no. 1, pp. WA1–WA11, Jan. 2016.

[16] R. N. Bohidar and J. F. Hermance, "The GPR refraction method," *Geophysics*, vol. 67, no. 5, pp. 1474–1485, Sep. 2002.

[17] E. Forte, M. Dossi, M. Pipan, and R. R. Colucci, "Velocity analysis from common offset GPR data inversion: Theory and application to synthetic and real data," *Geophys. J. Int.*, vol. 197, no. 3, pp. 1471–1483, Jun. 2014.

[18] I. Iqbal *et al.*, "Near surface velocity estimation using GPR data: Investigations by numerical simulation, and experimental approach with AVO response," *Remote Sens.*, vol. 13, no. 14, p. 2814, Jul. 2021.

[19] J. van der Kruk, C. P. Wapenaar, J. T. Fokkema, and P. M. van den Berg, "Three-dimensional imaging of multicomponent ground-penetrating radar data," *Geophysics*, vol. 68, no. 4, pp. 1241–1254, 2003.

[20] R. Streich and J. van der Kruk, "Accurate imaging of multicomponent GPR data based on exact radiation patterns," *IEEE Trans. Geosci. Remote Sens.*, vol. 45, no. 1, pp. 93–103, Jan. 2007.

[21] G. Ludeno, I. Catapano, A. Renga, A. R. Vetrella, G. Fasano, and F. Soldovieri, "Assessment of a micro-UAV system for microwave tomography radar imaging," *Remote Sens. Environ.*, vol. 212, pp. 90–102, Jun. 2018.

[22] G. Gennarelli *et al.*, "A low frequency airborne GPR system for wide area geophysical surveys: The case study of Morocco desert," *Remote Sens. Environ.*, vol. 233, Nov. 2019, Art. no. 111409.

[23] C. Noviello, G. Esposito, G. Fasano, A. Renga, F. Soldovieri, and I. Catapano, "Small-UAV radar imaging system performance with GPS and CDGPS based motion compensation," *Remote Sens.*, vol. 12, no. 20, p. 3463, Oct. 2020.

[24] K. Wu *et al.*, "A new drone-borne GPR for soil moisture mapping," *Remote Sens. Environ.*, vol. 235, Dec. 2019, Art. no. 111456.

[25] S. Lambot, E. C. Slob, I. V. D. Bosch, B. Stockbroeckx, and M. Vanclooster, "Modeling of ground-penetrating Radar for accurate characterization of subsurface electric properties," *IEEE Trans. Geosci. Remote Sens.*, vol. 42, no. 11, pp. 2555–2568, Nov. 2004.

[26] S. Lambot and F. André, "Full-wave modeling of near-field radar data for planar layered media reconstruction," *IEEE Trans. Geosci. Remote Sens.*, vol. 52, no. 5, pp. 2295–2303, May 2014.

[27] C. A. Balanis, *Antenna Theory: Analysis and Design*, 4th ed. Chichester, U.K.: Wiley, 2005.

[28] A. R. Mallahzadeh and F. Karshenas, "Modified TEM horn antenna for broadband applications," *Prog. Electromagn. Res.*, vol. 90, pp. 105–119, 2009.

[29] S. Lambot, L. Weihermller, J. A. Huisman, H. Vereecken, M. Vanclooster, and E. C. Slob, "Analysis of air-launched ground-penetrating radar techniques to measure the soil surface water content," *Water Resour. Res.*, vol. 42, no. 11, pp. 1–12 Nov. 2006.

[30] K. Z. Jadoon, S. Lambot, E. C. Slob, and H. Vereecken, "Analysis of horn antenna transfer functions and phase-center position for modeling off-ground GPR," *IEEE Trans. Geosci. Remote Sens.*, vol. 49, no. 5, pp. 1649–1662, May 2011.

[31] S. Lambot, M. Antoine, M. Vanclooster, and E. C. Slob, "Effect of soil roughness on the inversion of off-ground monostatic GPR signal for noninvasive quantification of soil properties," *Water Resour. Res.*, vol. 42, no. 3, pp. 1–10, Mar. 2006.

Kaijun Wu received the M.Sc. degree in geophysics from Central South University, Changsha, China, in 2018. She is currently pursuing the Ph.D. degree in agricultural and environmental engineering from the Université catholique de Leuven (UCLouvain), Leuven-la-Neuve, Belgium.

Her research interests include subsurface imaging, electromagnetic modeling for ground-penetrating radar, and inversion for nondestructive characterization of soils and materials.

Sébastien Lambot (Member, IEEE) received the M.Sc. *(magna cum laude)* and Ph.D. *(summa cum laude)* degrees in agricultural and environmental engineering from the Université catholique de Leuven (UCLouvain), Leuven-la-Neuve, Belgium, in 1999 and 2003, respectively.

From 2004 to 2005, he was a European Marie-Curie Post-Doctoral Scientist with the Delft University of Technology, Delft, The Netherlands. From 2006 to 2012, he was a Research Group Leader with Forschungszentrum Jülich, Jülich, Germany. Since 2006, he has been a Professor and an FNRS Research Group Leader with UCLouvain. He has authored or coauthored more than 100 journal articles on these topics. His research interests include electromagnetic modeling for ground-penetrating radar (GPR) and electromagnetic induction, inversion for nondestructive characterization of soils and materials, hydrogeophysics, and remote sensing of the environment.

Dr. Lambot was a General Chair of the 3rd International Workshop on Advanced GPR in 2005 and the General Chair of the 15th International Conference on GPR in 2014. He has Organized GPR and Hydrogeophysics Sessions in the GPR, IWAGPR, AGU, EGU, CMWR, and EAGE international conferences. He was a Guest Editor for four Special Issues in *Near Surface Geophysics*, the *Vadose Zone Journal*, and the IEEE JOURNAL OF SELECTED TOPICS IN APPLIED EARTH OBSERVATIONS AND REMOTE SENSING (JSTARS). He was an Associate Editor of the *Vadose Zone Journal* from 2009 to 2014. He was also an Associate Editor of the IEEE JSTARS.